Sequences of dislocation reactions and helicity transformations in tubular crystals

Andrei Zakharov [1,2] and Daniel A. Beller [3,*]

[1]*Department of Materials Science and Engineering, University of Pennsylvania, Philadelphia, Pennsylvania 19104, USA*
[2]*Department of Physics, University of California, Merced, California 95343, USA*
[3]*Department of Physics and Astronomy, Johns Hopkins University, Baltimore, Maryland 21218, USA*

Freestanding tubular crystals offer a general description of crystalline order on deformable surfaces with cylindrical topology, such as single-walled carbon nanotubes, microtubules, and recently reported colloidal assemblies. These systems exhibit a rich interplay between the crystal's helicity (the chiral angle) on its periodic surface, the deformable geometry of that surface, and the motions of topological defects within the crystal. Previously, in simulations of tubular crystals as elastic networks, we found that dislocations in nontrivial patterns can costabilize with kinks in the tube shape, producing mechanical multistability. Here, we extend that work with detailed Langevin dynamics simulations in order to explore defect dynamics efficiently and without the constraints imposed by elastic network models. Along with the predicted multistability of dislocation glide, we find a variety of irreversible defect transformations, including vacancy formation, particle extrusions, and "reactions" that reorient dislocation pairs. Moreover, we report spontaneous sequences of several such defect transformations, which are unique to tubular crystals. We demonstrate a simple method for controlling these sequences through a time-varying external force.

I. INTRODUCTION

Freestanding tubular crystals represent a distinctive form of crystal structure found in both natural and technological settings. Characterized by their hollow, tubelike morphology, tubular crystals consist of atoms or molecules arranged in a two-dimensional (2D) lattice structure closed along one direction into the topology of a cylinder. Unlike a 2D crystal attached to a cylindrical substrate [1–5], tubular crystals define their own tubular surface, allowing them to freely deform by distorting out of the tangent plane [6,7]. Examples of freestanding tubular crystals include single-walled carbon nanotubes (SWCNTs) [8,9], capsids of filamentous viruses [10], microtubules [11], and self-assemblies of DNA origami colloids [12]. The emergence of such crystals has sparked significant interest due to their exceptional mechanical, electrical, and optical properties and their potential applications in nanoscience [8,9], functional materials [13,14], and biotechnology [15,16].

Similar to other crystals, tubular crystals can contain lattice defects, such as grain boundaries and dislocations. These imperfections naturally arise due to various factors including crystal growth kinetics, lattice mismatch with supporting substrates, or external influences, and they play a significant role in determining the tubular crystal's response properties [17,18]. Controlling the number of defects and their dynamics is not only important for predicting crystal properties and tailoring them for applications, but it also provides pathways for synthesizing programmable structures [19]. In particular,

the movement of dislocations alters the helicity of the tubular crystal, which in turn affects properties such as electrical conductivity [6] and growth kinetics [4,20,21].

In prior work [19], we investigated the mechanics of dislocations in flexible, freestanding tubular crystals using a zero-temperature elastic network model. In that setting, dislocation test moves occurred through discrete, imposed bond flips in a network of harmonic springs, and the system evolved to minimize its total energy. This model predicted that dislocations could costabilize with kinks in the tube axis, introducing mechanical multistability in tube shape, such that certain imposed dislocation patterns allowed for programmable tube conformations and tunable mechanical response.

However, the assumptions of the elastic network model exclude some phenomena likely to be of interest in colloidal crystals [22,23]. Because the model probes dislocation motions by imposed bond flips, one defect at a time, it is challenging to investigate other types of possible particle rearrangements such as vacancy formation, extrusion of particles from the crystal surface, and the interaction of existing dislocations with spontaneously nucleated defect pairs in dislocation "reactions."

Here, we use Langevin dynamics simulations to investigate the spontaneous evolution of tubular crystals with thermal fluctuations and without constraints on the particles' contact network. Our simulated particles interact through a model anisotropic interaction potential that stabilizes sheetlike assemblies. Such particles with designed surface patterns can be precisely engineered, for example by colloidal fusion [24] or DNA-coating of colloids [25,26], and they have demonstrated promise in the directed self-assembly of 2D and 3D structures using these particles as building blocks [27–30]. We
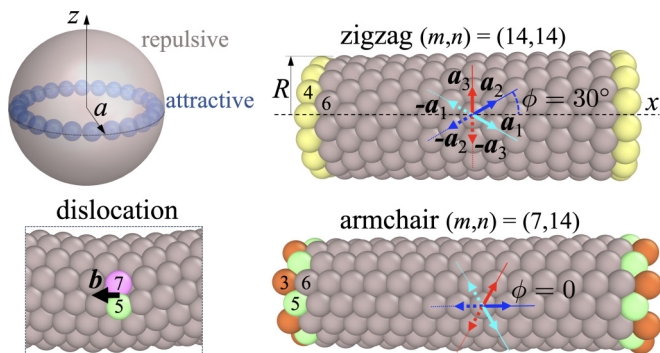
---

*d.a.beller@jhu.edu

FIG. 1. Construction of freestanding tubular crystals. Tubular crystals (examples shown at right) are made up of patchy particles (upper left panel), each composed of a primary, sterically repulsive sphere and several attractive spheres. In the tube's local tangent plane, the particles form a close-packed hexagonal lattice, with primitive lattice directions $\pm\mathbf{a_1}$, $\pm\mathbf{a_2}$, $\pm\mathbf{a_3}$. The crystal's helicity is characterized by the chiral angle ϕ between the tube axis x and the steepest left-handed helical lattice direction or *parastichy*, labeled $\mathbf{a_2}$ (upper right panel). Example tubular crystals shown are the achiral types: "zigzag," with $\phi = 30°$, and "armchair," with $\phi = 0°$. The number of distinct parastichies along $\pm\mathbf{a_1}$ (the steepest right-handed helices) and along $\pm\mathbf{a_2}$ give the parastichy numbers (m, n). Particles are colored (and in some instances labeled) by coordination number, with gray identifying the sixfold-coordinated particles of a pristine hexagonal packing. A pair of fivefold- and sevenfold-coordinated particles forms a dislocation (bottom left panel), and their separation vector is perpendicular in the local tangent plane to the dislocation's Burgers vector $\mathbf{b}$.

initialize our systems with various tubular crystal configurations, including both chiral and achiral states.

Although the elastic network model's predictions are often corroborated here, we additionally observe a wealth of more complex behaviors when dislocations pass near each other, including vacancy formation and particle extrusion. Most interestingly, we report novel dislocation reaction sequences that are unique to the tubular crystal setting, arising from the fact that distances between gliding dislocations change non-monotonically due to the surface's periodicity. We show that the interplay between dislocations, the helical symmetry of tubular crystals, and out-of-tangent-plane deformations leads to a rich variety of transformations in crystal structure, including metastable dislocation patterns, dislocation reactions, and helicity transformations.

II. METHODS: PARTICLES AND TUBULAR ASSEMBLIES

We construct simulated tubular crystals using collections of identical, spherical, patchy particles. The patchy particles exhibit short-range attraction only along a narrow equatorial band on their surfaces, and otherwise interact only through steric repulsion. These anisotropic surface interactions are chosen to stabilize sheetlike assemblies. We construct each patchy particle from one purely repulsive sphere of effective radius a and, centered at the same point, an attractive patch comprising a circular arrangement of small spheres, whose centers sit at a radius $a - \delta$ that places them just inside the repulsive sphere (Fig. 1). (More general interactions can be

engineered using other arrangements of attractive spheres, such as sinusoidal paths [27].) The large, repulsive sphere and smaller, attractive spheres making up a given patchy particle move together as a rigid body.

Repulsion between the large spheres of different patchy particles separated by center-to-center distance r is determined by the Weeks-Chandler-Andersen (WCA) potential [31], a truncated and shifted Lennard-Jones (LJ) potential [32] given by

$$E_r(r) = \begin{cases} 4\varepsilon_r\left[\left(\frac{\sigma}{r}\right)^{12} - \left(\frac{\sigma}{r}\right)^6\right] + \varepsilon_r & \text{if } r \leqslant 2^{1/6}\sigma, \\ 0 & \text{otherwise.} \end{cases} \quad (1)$$

Here, ε_r is the interaction strength and $\sigma = 2a/2^{1/6}$ sets the truncation distance to $r = 2a$, equal to the minimum of the LJ potential, so that $E_r(r)$ is purely repulsive and has a slope that goes to zero at the truncation distance.

The pair interactions between attractive spheres on different patchy particles are defined by the soft potential

$$E_a(r) = \begin{cases} -\varepsilon_a[1 + \cos(\pi r/r_a)] & \text{if } r \leqslant r_a, \\ 0 & \text{otherwise} \end{cases} \quad (2)$$

with strength ε_a and range r_a. The repulsive and attractive spheres have no direct interactions.

We note that the choice of Eqs. (1) and (2) as model potentials is not unique, and we have confirmed that some alternative models, such as Morse and Coulomb potentials, lead to behaviors in qualitative agreement with the results reported below. While the Lennard-Jones potential serves as a simplified phenomenological representation of atomic-scale interactions, it is also widely used for simulated interactions between larger-scale objects such as proteins and colloids with successful comparison to experimental observations [33–35].

We explore Langevin dynamics with these pair interactions by performing molecular dynamics (MD) simulations in LAMMPS [36]. We use scaled Lennard-Jones units: each patchy particle has unit mass ($m_p = 1$), damping ($\gamma = 1$), and steric repulsion strength ($\varepsilon_r = 1$). The temperature is held fixed at $k_B T = 0.1$ using a Nosé-Hoover thermostat. Because each patchy particle is treated as a rigid body, the translation and rotation of its constituent large and small spheres are calculated according to the net force and torque acting upon them collectively.

The anisotropy of patchy particles allows for their assembly into sheets [27], and then into higher-energy tubular structures when a sheet is rolled up in one direction. In this work, we do not consider the self-assembly process; instead, we construct initial conditions consisting of single-layer tubular crystals of given geometry, helicity, and preexisting defects. In particular, we set the initial center positions of the patchy particles to be the node locations of a tubular hexagonal lattice containing a pair of separated dislocations, obtained using the elastic network simulations reported in Ref. [19]. Each patchy particle is oriented so that its equatorial attractive band lies in the tube's local tangent plane. The initial center-to-center separation $2r$ of neighboring patchy particles is close to the patchy particle diameter $2a$, so the patchy particles begin in contact and stick together laterally. However, the imposed initial configuration is not necessarily a mechanical equilibrium state for the patchy particles; in

particular, initial dislocation positions may be unstable. In many cases, we observe large-scale deformations in the tube shape accompanied by the motion of preexisting dislocations.

The tubular arrangement of particles can be conveniently described using the parastichy numbers, a pair of integers (m, n) defining the number of distinct helices of particles in the steepest right-handed and steepest left-handed directions [37]. In the family of helices there are three principal directions along unit vectors $\pm\mathbf{a}_i$, $i = 1, 2, 3$. To describe the helicity of a tubular crystal, we use the chiral angle ϕ between the steepest left-handed helix along the $\mathbf{a}_2$ direction and the tube axis (Fig. 1, upper right panel). Each elementary dislocation in the lattice is composed of a positive disclination at a fivefold-coordinated particle and a negative disclination at a sevenfold-coordinated particle. It can be characterized by a Burgers vector $\mathbf{b}$ of length a orthogonal to the line connecting the five–seven disclination pair (Fig. 1, bottom left panel).

To keep the parameter space tractable, we specialize to tubes with an armchair and near-armchair crystal configuration, i.e., having one lattice direction approximately parallel to the tube axis, and thus ϕ near $0°$ or $60°$. These helicities are the most commonly observed type in carbon nanotubes (CNTs) [20,38]. When subjected to applied torsion, which we explore below, armchair tubular crystals exhibit large deformations and dislocation pair nucleation [39]. In contrast, zigzag tubular crystals (the other achiral type, with $\phi = 30°$) have one lattice direction oriented circumferentially, and thus they can more easily accommodate the shear stress caused by torsion via circumferential slip. Chiral tubes of general helicity include intermediate configurations between the two achiral cases, separated by discrete changes in the chiral angle $\Delta\phi = 30°/m$.

The constructed tubular crystals are free-standing, meaning that the tube's radius can change locally to reduce the energy associated with interparticle attraction and repulsion. For our patchy particles with equatorial attractive bands, the minimum-energy configuration is a flat monolayer with regular hexagonal close packing. In tubular assemblies, every configuration has nonvanishing potential energy due to the curvature of the monolayer. The preference for a flat sheet morphology introduces a bending energy, given approximately by $F_{\text{bend}} \approx \pi\kappa L/R$, for a tube of length L, radius R, and effective bending stiffness κ. Whereas κ was imposed as a mean curvature modulus in our previous elastic network model [7,19], here the bending rigidity emerges from the anisotropic interactions and depends on the strength of attractive and repulsive potentials $(\varepsilon_a, \varepsilon_r)$, as well as the tube chiral angle ϕ. Prior studies have shown that the effective bending rigidity of zigzag tubes is higher than in their armchair counterparts because the former have a larger number of bonds oriented in the bending plane [40,41].

In our simulations, we choose attractive potentials strong enough ($\varepsilon_a = 0.1$) to prevent disintegration of the structure due to the thermal fluctuations. On the other hand, we also avoid making the potentials so strong that the tube develops capping [42] at the free ends (observed at $\varepsilon_a \geqslant 0.2$, $\varepsilon_r = 1$) or becomes faceted into planar regions joined at creases (at $\varepsilon_a \geqslant 0.5$, $\varepsilon_r = 1$). At sufficiently large effective bending stiffness, this faceting reduces the bending energy by localizing it at the creases [43–46]. Although a comprehensive

exploration of the $(\varepsilon_a, \varepsilon_r)$ parameter space is outside the scope of this work, we expect that increasing the attraction strength ε_a will stabilize the tubular crystal against thermal fluctuations by strengthening the interparticle forces, and that the effective bending rigidity will increase with increasing repulsion strength ε_r.

The ends of our simulated tubes are free, facilitating the absorption of dislocations into the boundaries and simplifying the construction of tubes with spatially varying parastichy numbers, i.e., with different chiral angle at opposite ends. To reduce the influence of free boundaries on the dislocation interactions of interest, we construct the tubes to be relatively long, typically more than 25 times larger than the tube radius. The undercoordinated (dangling) patchy particles at the tube ends, depicted as colored spheres in the right-hand panels of Fig. 1, localize the energy that effectively represents boundary tension. We keep temperature low enough to prevent this tension from causing shrinkage and crumpling of the tube edges [47,48], due to the tendency of undercoordinated particles to establish new bonds. We note that in an alternative scenario with periodic boundaries along the tube axis direction, there would be no means by which dislocation pairs with nonzero climb separation could be removed from the crystal through glide moves, introducing additional complexity to the landscape of metastable defect configurations.

III. RESULTS

A. Dislocations spontaneously react in a freestanding tubular crystal

First, we explore the stability of a freestanding tubular crystal with an armchair $(m, n) = (7, 14)$ arrangement of particles and containing two oppositely oriented, isolated dislocations with Burgers vectors $\pm\mathbf{b}$ (Fig. 2). This configuration, while containing a net-zero Burgers vector "charge," requires a phyllotactic transition in which (m, n) differs in the region between the dislocations compared to outside them, by an amount depending on the orientation of $\mathbf{b}$.

In Fig. 2, we plot a stability map describing the evolution of two dislocations with Burgers vectors along (or opposite to) the axial direction, depending on the axial component $g\times a$ and azimuthal component $c\times a$ of separation between the defects, where g and c are integer numbers of glide and climb steps, respectively. When dislocations move, they do so exclusively in glide motions along their Burgers vectors, as this is energetically cheaper than climb motion along other directions and requires no change in the total number of particles. As the Burgers vectors lie along the tube axis in this example, the defect motions recorded in Fig. 2 are only along the axial direction; the azimuthal separation remains fixed. For larger azimuthal separations, the dislocations glide to decrease their axial separation to zero.

Even though the middle region of the tube has a larger radius with lower bending energy, the dislocations are attracted to a state with minimum axial separation at most possible azimuthal separations. The resulting tube conformation contains a kink in the tube axis, as observed in the elastic network model [19]. This interaction is observed for axial separations close to πR when the azimuthal separation is around πR,
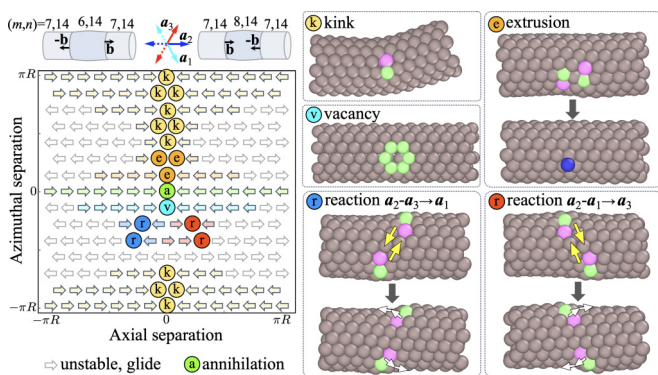
FIG. 2. A stability map (left) for two interacting dislocations oriented along the tube axis ($\pm\mathbf{a}_2$ parastichies) in an armchair tube [$(m, n) = (7, 14)$, $\phi = 0$] at different values of azimuthal (climb) separation. The region of the tube between the dislocations has a different tessellation, $(m, n) = (6, 14)$ or $(8, 14)$. Unstable states are indicated by wide arrows, colored according to the type of metastable state toward which they evolve (circles), if any. If the axial separation is larger than πR (outside the plotted region), dislocations repel weakly and glide toward the tube ends. Labels for metastable state types correspond to representative tube configurations depicted at right, which show only portions of the tubes containing the defects. Green, magenta, and blue particles are, respectively, fivefold-coordinated, sevenfold-coordinated, and extruded.

but the interaction range decreases as azimuthal separation decreases.

The outcome changes significantly if the azimuthal (climb) separation is small, $|c| \leqslant 3$. We can divide this regime into two parts, one with $c > 0$ where the fivefold-coordinated particles are closer to the other dislocation ("fives inside"), and one with $c < 0$ where the sevenfold-coordinated particles are closer ("sevens inside"). For the fives inside case, the two dislocations attract to zero axial separation and then disappear through an *extrusion* event, in which one or more particles are expelled from the surface of the tubular crystal and forced to sit on top of it, at larger radius. For $c = 1$, a single particle is extruded, becoming a threefold-coordinated particle (colored blue in the "extrusion" panel of Fig. 2) adjacent to three sevenfold-coordinated particles under it (colored gray to show pristine arrangement in the tube tangent plane). The total number of bonds is conserved in this extrusion. Dislocations separated by $c = 2$ climb steps cause an extrusion of two particles at small axial separation.

An opposite azimuthal separation, with $c = -1$ and "sevens inside," leads instead to the formation of a *vacancy*. The total number of bonds decreases, leaving six fivefold-coordinated particles that become a nucleation site for plastic deformations when an external force is applied. For example, applied torsion can destabilize this metastable vacancy, replacing it with two dislocations oriented along a lattice direction that depends on the sign of the torsion: Simulations show that unlike a pristine tube under torsion, in which unbinding dislocations have Burgers vectors $\pm\mathbf{a}_2$, the preferable path for nucleation in a tube with a vacancy is along $\pm\mathbf{a}_1$ when the torsion is applied in the clockwise direction, and along $\pm\mathbf{a}_3$ when torsion is in the counterclockwise direction (Supplemental Material videos 1-2 [49]).
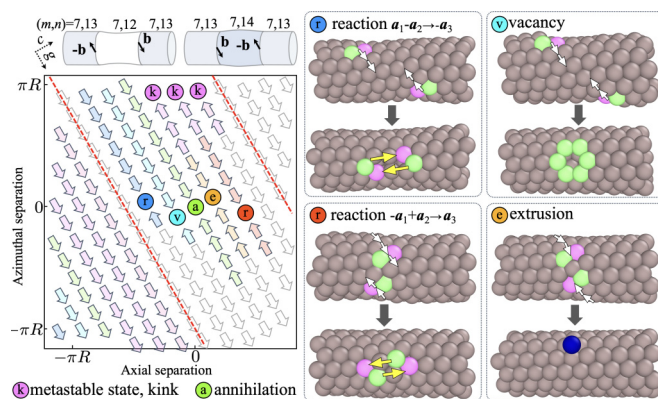

FIG. 3. Left: A stability map for two interacting dislocations spontaneously gliding along helical trajectories ($\pm\mathbf{a}_1$ parastichies) in a near-armchair tube with $(m, n) = (7, 13)$, $\phi \approx 2.5°$, at various values of climb separation c. If the dislocations are initially at negative axial separation, then the central region of the tube has $(m, n) = (7, 12)$ and decreased radius, and the dislocations are attracted (colored arrows) to one or more metastable states (colored circles) at small axial separation. The exception to this rule is a single path at $c = -3$ (dashed red line). Right: portions of the tubes containing the defects are shown at representative defect transformation events.

While the vacancy formation at $c = -1$ is intuitively opposite to the extrusion at $c = +1$, we find an altogether new behavior for $c = -2$ or -3: When the gliding dislocations reach points that sit on the same $\pm\mathbf{a}_3$ parastichy, their Burgers vectors appear to suddenly change from $\pm\mathbf{a}_2$ to $\pm\mathbf{a}_1$. This is a dislocation *reaction* event [50–52]. As explored in detail below, we can understand this process as resulting from the nucleation of a new dislocation pair with Burgers vectors $\pm\mathbf{a}_3$. The new dislocations glide apart along the $\pm\mathbf{a}_3$ parastichy until each new dislocation reacts with one of the original dislocations, leaving behind two dislocations with resultant Burgers vectors $\pm\mathbf{a}_2 + (\pm\mathbf{a}_3) = \pm\mathbf{a}_1$. After the reaction, the $\pm\mathbf{a}_1$ dislocations glide only a few steps before coming to rest in a metastable state. The mirror-image process is also observed, with dislocations of initial Burgers vector $\pm\mathbf{a}_2$ and separation along a $\pm\mathbf{a}_1$ parastichy reacting to become dislocations with Burgers vectors $\pm\mathbf{a}_3$.

In this tube with $(m, n) = (7, 14)$, there is only a single azimuthal separation, at $c = 4$ climb steps, at which the dislocations are always repulsive and do not react. At zero azimuthal separation and axial separation less than πR, dislocations are attractive and annihilate, forming a pristine tube.

More generally, the glide paths of dislocations in tubular crystals are helices rather than straight lines, a distinction that we find has important consequences for defect interactions. In Fig. 3 we show a stability map for a near-armchair tubular crystal, $(m, n) = (17, 13)$, with two dislocations whose Burgers vectors ($\mathbf{b}_{1,2} = \pm\mathbf{a}_1$) make the glide paths helical. At large positive or negative axial separation Δx, the dominant trend is simply for Δx to steadily increase. Unlike the previous example with dislocations along the tube axis ($\pm\mathbf{a}_2$), here the helicity transition ($\Delta m, \Delta n$) induced by these defects' relative glide motion causes regions of larger radius to grow, at the expense of regions of smaller radius, as Δx increases, due to the bending energy.

However, once dislocations reach smaller axial separation, they usually interact in a more complex way that stabilizes their relative positions. We find two groups of these metastable states at small Δx. In the first group, dislocation pairs come to rest at maximum azimuthal separation Δy (i.e., opposite sides of the tube), giving the tube a kinked conformation. The other group, at small azimuthal separation, results in more dramatic changes to the defects, strongly depending on the climb separation c between the two glide paths. For $c = 0$, the dislocations annihilate, just as in the previously examined case of **b** parallel to the tube axis. For $|c| = 1$, the final state has no dislocations but contains either a vacancy ($c = -1$, sevens inside) or a single extruded particle ($c = +1$, fives inside).

Examining the $|c| = 2$ paths, we find that dislocation reactions may occur for both sevens-inside and fives-inside configurations, in contrast to the previous example with Burgers vectors parallel to the tube axis. The reactions in this case replace the $\pm\mathbf{a}_1$ Burgers vectors with new ones along $\pm\mathbf{a}_3$. For $c = +2$, there are two different metastable states along the same glide path: the "reacted" state with two nearby $\pm\mathbf{a}_3$ dislocations in an approximately straight tube, and a "kinked" state with diametrically opposed $\pm\mathbf{a}_1$ dislocations.

For this particular choice of initial parastichy numbers $(m, n) = (7, 13)$, there is only one climb separation $c = -3$ (highlighted with a dashed red line along the helical path in the stability map in Fig. 3) that allows two dislocations to "miss" each other, gliding past $\Delta x = 0$ to $\Delta x \to +\infty$ without any metastable state. We expect that the number of such free paths will be greater for tubes with larger (m, n).

B. Applied torsion causes sequences of defect-mediated transformations

To better understand how helicity transitions in tubular crystals may be controlled, we next examine the effects of externally imposed torsion applied to the tube. For that purpose, in our MD simulations two rings of particles located far enough from the existing defects are grouped, and torque is applied on each group around its center of mass using the standard addtorque command in LAMMPS. Just as an applied shear stress provides control over an isolated dislocation's motion in a planar crystal [52], here torsion imposed at the tube ends produces shear stress in the tube's tangent plane and thus a Peach-Koehler force on the dislocations [53]. Because we are particularly interested in switching between mechanically metastable states, we study in detail the multistable glide path identified above in the $(m, n) = (7, 13)$ tube, with $c = +4$ climb separation. We find that we can switch between the reacted and kinked metastable states by means of this applied torsion. Moreover, the transition is reversible through reversal of the torsion direction. While the kinked state has higher energy than the reacted state, we can impose a torsion sufficiently strong that the "reacted" dislocations undergo a reverse reaction from their $\pm\mathbf{a}_3$ Burgers vectors back to their original $\pm\mathbf{a}_1$ orientations and then glide to the metastable kinked state.

To quantitatively analyze this mechanical reconfigurability, we plot in Fig. 4 the change in the tube's total potential energy as the applied torsion is increased monotonically with
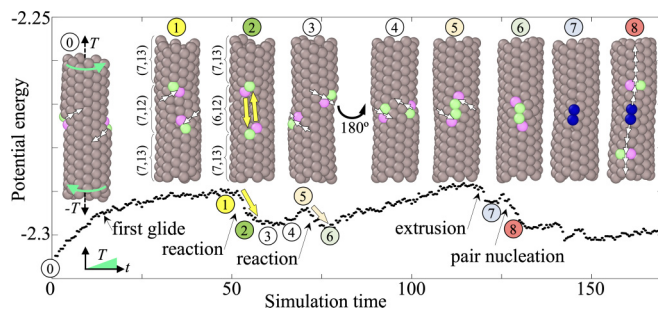

FIG. 4. Evolution of the potential energy during a sequence of spontaneous dislocation glide, reaction, extrusion, and pair-unbinding events in a near-armchair tube under applied torsional force T. The initial state 0 is metastable, containing two dislocations with Burgers vectors oriented at angle $\theta \approx -\pi/3$ with respect to the tube axis. Applied torsion linearly increases with time. The final state has two extruded particles (blue), an altered helicity $(m, n) = (6, 13)$ throughout the tube, and no dislocations once those in state 8 glide apart to the ends of the tube. Insets depict only the region of interest within a longer tube, at each labeled time; the view is rotated 180° between states 3 and 4, and is otherwise held fixed.

time. We take the $c = +4$ metastable kink state of Fig. 3 as the initial configuration and apply torsion to the tube as illustrated in the state 0 panel of Fig. 4. The magnitude T of imposed torsion linearly increases with simulation time t as $T = 250 + 0.25t$ (LJ units). As simulation time progresses, we find not only an escape from the metastable kink state into the reacted state, but also a series of subsequent events including extrusion and other reactions. Representative states from this sequence of transitions are shown as inset panels in Fig. 4.

At first, applied torsion leads to an increasing potential energy and destroys the metastable state, inducing glide (at $t = 15$), which reduces the positive rate of change of the energy. As the dislocations glide apart along helical trajectories, they increase their axial separation but eventually bring their azimuthal separation to near zero (state 1 at $t = 50$, Supplemental Material video 3 [49]). At that time, with the dislocations located on the same $\pm\mathbf{a}_2$ parastichy, a dislocation reaction event occurs rapidly. The reaction changes the two Burgers vectors from $\pm\mathbf{a}_1$ to $\pm\mathbf{a}_3$ and thus changes the parastichy numbers describing the middle region of the tube from (7,12) to (6,12) (state 2 at $t = 55$). The potential energy drops sharply with this reaction event. Subsequently, with their new helical $\pm\mathbf{a}_3$ glide paths, the dislocations continue to glide with the azimuthal components favored by the applied torsion while also decreasing their axial separation, which allows a reduction in the size of the tube's narrower central region and thus a reduction in bending energy. Eventually, the dislocations approach each other again on the opposite side of the tube (state 4 at $t = 70$), where they react a second time and obtain Burgers vectors $\pm\mathbf{a}_1$ (state 6 at $t = 80$). In this state, the two positive disclinations are in contact, creating a large compressive force that obstructs further motions of the dislocations for some time. Continuing increase in the applied torsion causes a gradual increase in potential energy and, eventually, an extrusion of two particles takes place (state 7 at $t = 120$). Finally, the extruded particles become a nucleation

point for a pair of dislocations along the $\pm \mathbf{a}_2$ directions (state 8 at $t = 130$).

This example demonstrates that dislocation reactions decrease the elastic energy in a tubular crystal through re-orientation of existing dislocations when torsion is applied. Although the hexagonal crystal structure imposes limitations on the available glide motion and reaction directions, specifically along the three lattice directions $\pm \mathbf{a}_{1,2,3}$, the tube's periodicity enables a sequence of reactions. In planar crystals, the spatial separation between a pair of dislocations varies monotonically with their glide motion. In contrast, the tube's periodicity facilitates multiple reaction events: After the initial reaction, dislocations glide apart along helical paths but eventually become closer again on the opposite side of the tube, leading to further reactions.

C. Analytical energy approximation explains dislocation movements and reactions

To better understand why we observe some possible re-actions and not others in MD simulations, we examine an analytical approximation for the dislocation pair interaction energy $\mathcal{F}_{\text{int}}$ on a cylinder of fixed radius R, calculated in [54] under the assumptions of isotropic continuum elasticity. The pair interaction energy was calculated by integration of the Peach-Koehler force $F_i = b_k \sigma_{jk} \varepsilon_{ijz}$ (summing over $j, k = x, y$) for a dislocation of Burgers vector $\mathbf{b}$ experiencing a stress tensor σ. This stress tensor was in turn calculated by summing the stresses sourced by the other dislocation along with its infinite periodic images in the cylindrical space, by means of a Sommerfeld-Watson transformation. For two antiparallel dislocations with axial separation x and azimuthal separation y on a tube of radius R, the predicted interaction energy takes a general form [7]

$$\mathcal{F}_{\text{int}}(\tilde{x}, \tilde{y}, \theta) = \frac{Ya^2}{2\pi} \left\{ \ln[\cosh \tilde{x} - \cos \tilde{y}] \right.$$
$$+ \tilde{x} \left[\frac{\sinh \tilde{x} \cos(2\theta) + \sin \tilde{y} \sin(2\theta)}{\cos \tilde{y} - \cosh \tilde{x}} \right]$$
$$\left. + \frac{R}{a} [\tilde{\sigma}_{xy}(\tilde{y} \sin \theta - \tilde{x} \cos \theta)] \right\}, \quad (3)$$

where $\tilde{x} = x/R$, $\tilde{y} = y/R$, θ is the angle between either dislocation's Burgers vector and the tube axis, Y is the two-dimensional Young's modulus, a is one-half of the lattice spacing, and $\tilde{\sigma}_{xy} = (4\pi/Y)\sigma_{xy}$ is the constant, nondimensionalized applied shear stress. The calculation omits the Peierls barrier to glide steps [53] and assumes that the crystal is wrapped around a rigid cylindrical surface, in contrast to the freestanding tubular crystals in our study. Additionally, the bending energy favoring larger tube radius plays no role in the rigid-cylinder calculation. Nonetheless, the comparison is qualitatively illuminating when we examine one-dimensional cuts, representing parastichies, through the predicted two-dimensional interaction energy landscapes.

To illustrate the usefulness of the analytical approximation, in Fig. 5(a) we present interaction energy landscapes predicted by Eq. (3) for two dislocations of unit Burgers vectors at constant angles to the tube axis $\theta = -\pi/3, 2\pi/3$ (corresponding to gliding along the principal orientations $\pm \mathbf{a}_1$ in an armchair
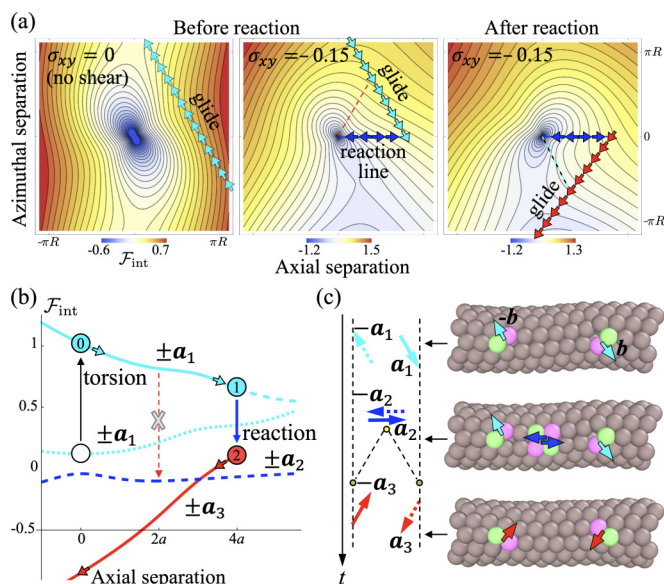

FIG. 5. Analytical approximations for interaction energies of a reacting dislocation pair on an armchair tubular crystal. (a) Calculated interaction energy landscape, $\mathcal{F}_{\text{int}}$, overlayed with paths of relative glide. During the reaction, the dislocations' Burgers vectors change from $\pm \mathbf{a}_1$ to $\pm \mathbf{a}_3$, without changing their climb separation $c = 4$. Without applied torsion ($\sigma_{xy} = 0$, left panel), the dislocations are attracted to a stable state at zero axial separation. That state is destabilized by a shear stress $\sigma_{xy} = -0.15$ due to torsion, which causes the dislocations to glide apart and eventually react at zero azimuthal separation (center panel). Subsequently, the rotated defects glide in a different direction (right panel). (b) Interaction energy along the glide paths depicted in (a). The metastable state (white circle) in the zero-torsion path (cyan dotted curve) becomes unstable when torsion is applied, and the dislocations glide (cyan solid curve) from state 0 to state 1, where they react into a new state 2 and then glide along another glide path (red solid line). Possible but energetically unfavorable glide paths and reactions are shown by dashed curves and a dashed arrow, respectively. (c) A schematic diagram and representative states for the reaction event. In a tube under torsion, an extra pair of dislocations spontaneously nucleates and quickly unbinds between two existing dislocations, gliding toward and eventually reacting with them. After the reaction, the tube contains one pair of dislocations but with altered Burgers vector orientations, and the helicity of the region between the dislocations is altered.

tube lattice), before and after application of an external shear stress σ_{xy}. Without shear stress [Fig. 5(a), left panel], dislocations at any position along the glide path will glide (arrows) to a stable state with minimal axial separation to minimize the bending energy. Although the analytical theory [7,54] accounts only for the in-plane stresses, it correctly predicts the direction of dislocation glide that leads to the family of states at smaller axial separation.

Applied shear stress changes the analytical energy landscape, destabilizing the states at small axial separation, and predicting glide motion that increases the axial separation [cyan arrows in Fig. 5(a), middle panel], as we see in MD simulations. As a result, the dislocations glide along $\pm \mathbf{a}_1$ until reaching a common $\pm \mathbf{a}_2$ parastichy with minimal azimuthal

separation, and then they react along the $\mathbf{a}_2$ direction. This reaction rotates the Burger vectors by $\pi/3$ to a new pair of directions $\pm\mathbf{a}_3$. The calculation of Ref. [54] then predicts a different interaction energy landscape, which we show along with the new glide path (marked by red arrows) in the right panel of Fig. 5(a). As predicted analytically, the postreaction dislocations glide toward *smaller* axial separation under the same sign of applied torsion that pulled the original dislocation pair apart.

The energetic reasons for the observed dislocation glide and reaction behaviors become more apparent when we take one-dimensional cuts of the energy along the relevant parastichy paths. In Fig. 5(b) we plot the analytically predicted interaction energy along the glide paths before (cyan dotted curve) and after (cyan and red solid curves) applying an external torsion. Whereas an azimuthal separation of $-\pi R$ is metastable without applied torsion (open circle), the applied torsion creates a slope in the interaction energy that causes the dislocations to glide from state 0 to state 1 (cyan solid curve), corresponding to the glide motion along helical trajectories observed in our MD simulations (Fig. 4 state 0 to state 1). Prior to the observed reaction along a common $\mathbf{a}_2$ parastichy [blue arrows in Figs. 5(a) and 5(b)], the dislocations' $\pm\mathbf{a}_1$ glide parastichy brings them through a configuration with a common $\mathbf{a}_3$ parastichy at which they *could* react, but do not [red dashed line in Fig. 5(a), center panel]. Although this possible reaction would substantially decrease the predicted interaction energy [red dashed arrow in Fig. 5(b)], the system does not overcome the energy barrier associated with unbinding the reaction-mediating dislocation pair (explained in the next section) with $\mathbf{b} = \pm\mathbf{a}_3$ required to accomplish the reaction. Instead, the first reaction observed is at the common $\mathbf{a}_2$ parastichy. This observation is consistent with a prediction given in Ref. [7] for the Burgers vectors of dislocation pairs expected to spontaneously unbind in the presence of external torsion. In particular, for a tube with chiral angle $\phi = 0$ as in Fig. 5, the $\pm\mathbf{a}_2$ direction (blue arrows) is predicted to be more favorable for unbinding than the $\pm\mathbf{a}_3$ direction (cyan dashed line).

The reaction along the $\mathbf{a}_2$ direction reorients the Burgers vectors from $\theta = -\pi/3$ to $\theta = -2\pi/3 + \Delta$, where Δ is a small angle due to the helicity transition. This reorientation of Burgers vectors accompanies a decrease in the interaction energy [red solid curve in Fig. 5(b)] and a more negative slope of the energy with respect to glide (which now decreases rather than increases the axial separation). For comparison, we also plot the higher predicted interaction energy for the hypothetical situation in which the dislocations continue along $\pm\mathbf{a}_1$ without reacting [dashed cyan curve in Fig. 5(b)].

D. Spontaneous defect unbinding mediates dislocation reactions

To examine dislocation reactions in tubular crystals in greater detail, we increase the climb separation between the initial dislocations of Figs. 5(a) and 5(b) and apply external torsion to move the dislocations to a configuration where they undergo a reaction. This allows us to observe the mechanism of the reaction, and resulting changes in lattice helicity, over a larger region. In Fig. 5(c) we show simulated configurations and schematic representations of the dislocations

before, during, and after the reaction. Due to applied torsion, the dislocations with initial Burgers vectors $\pm\mathbf{a}_1$ glide apart until reaching a common $\pm\mathbf{a}_2$ parastichy. Then, we observe that a new, "reaction-mediating" dislocation pair with Burgers vectors $\pm\mathbf{a}_2$ nucleates midway along the common parastichy, with the net Burgers vector remaining zero, as it must. While the original dislocations remain stationary, the newly nucleated dislocations unbind analogously to Stone-Wales defect nucleation in graphene lattices [55] and glide toward the original defects until eventually combining with them. The reaction ends with a new configuration containing two dislocations with opposite Burgers vectors $\pm\mathbf{a}_3$ direction. This reoriented dislocation pair is not necessarily stable at its current separation, so the defects may next glide along their new $\pm\mathbf{a}_3$ helical glide paths to decrease the total energy.

We never observe dislocations with $|\mathbf{b}| > a$ in our simulations; all of the dislocations are elementary. A consequence of excluding larger Burgers vectors is that reactions by the mechanism we describe can never occur along the $\mathbf{b}$ direction, even if the dislocations sit on the same glide parastichy ($c = 0$), because a nucleated dislocation pair could only glide along such a path if its Burgers vectors were parallel to those of the original dislocation pair; the reaction would then produce nonelementary dislocations. (Geometrically, a reaction could occur that annihilates all dislocations, but this seems energetically implausible compared to the original dislocations simply gliding to zero separation and annihilating there.)

The final Burgers vectors are determined by the initial defects' orientations and the reaction-nucleated dislocations. For two oppositely oriented dislocations along $\pm\mathbf{a}_1$, a dislocation pair unbinding is possible along the other two primitive lattice directions $\pm\mathbf{a}_{2,3}$. The favorable direction for unbinding dislocations under torsional stress depends on the chiral angle ϕ [7]. For dislocations initially along $\mathbf{a}_1$, reactions will transform $\mathbf{a}_1 + \mathbf{a}_2 \rightarrow \mathbf{a}_3$ or $\mathbf{a}_1 + \mathbf{a}_3 \rightarrow \mathbf{a}_2$ (omitting the signs), where the energy barrier associated with unbinding along the $\mathbf{a}_3$ direction is larger than along $\mathbf{a}_2$, and thus is not favorable, as predicted in Ref. [7].

E. Alternating torsion allows manipulation of the chiral angle through dislocation reactions

Having demonstrated that externally imposed torsion can move dislocations into configurations where they react, we further demonstrate here that time-dependent torsion of alternating sign can be used to change the helicity of the tubular crystal. Such helicity changes hold significant practical implications, particularly in the field of carbon nanotubes (CNTs) to control their electrical conductivity [56,57]. Here we start with an achiral configuration with an armchair (7,14) tube containing two oppositely oriented dislocations along $\pm\mathbf{a}_2$, initially separated by $c = 3$ lattice spacings in the azimuthal direction (Fig. 6, state 1). As shown in Fig. 2, this state is unstable and the dislocations spontaneously glide apart to a state where they react along a $\pm\mathbf{a}_1$ parastichy, changing their orientation to $\pm\mathbf{a}_3$. However, by applying shear stress through torsion on the tube, we can prevent the reaction and instead force the defects to move in the opposite direction to a state (Fig. 6, state 2) that makes possible a reaction along a $\pm\mathbf{a}_3$

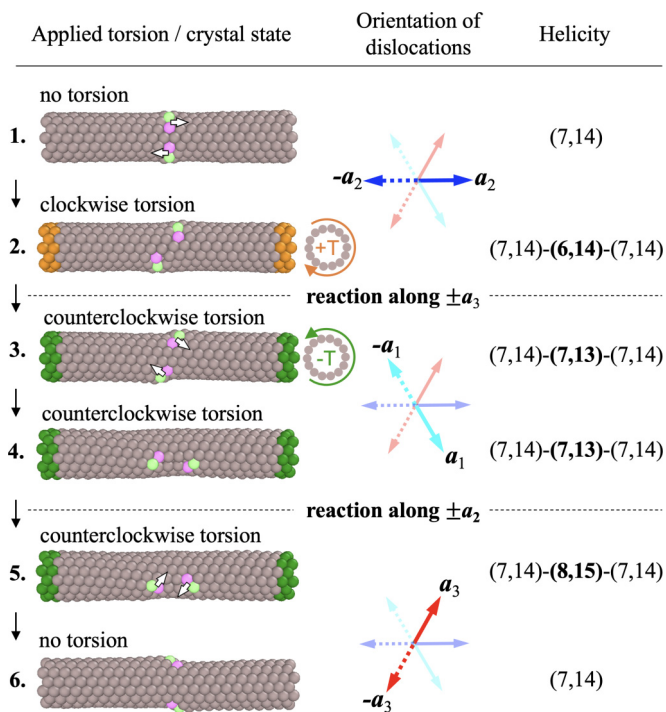| Applied torsion / crystal state	Orientation of dislocations	Helicity

FIG. 6. Transitions in dislocation orientation and crystal helicity through a sequence of reactions controlled by time-varying external torsion. Applying torsion in the clockwise direction (as viewed from outside the tube at either end) to the initial configuration with two dislocations along $\pm\mathbf{a}_2$ parastichy (state 1) leads to dislocation glide (state 2) and a reaction along the $\pm\mathbf{a}_3$ direction. Switching the direction of applied torsion (state 3) moves the dislocations closer to each other again (state 4), eventually leading to a reaction along the $\pm\mathbf{a}_2$ parastichy and a change of Burgers vectors to the $\pm\mathbf{a}_3$ direction (state 5). Finally, the dislocations glide to a metastable state at maximum azimuthal separation (state 6). Particles subject to applied torsion in the clockwise or counterclockwise direction are colored in orange and green, respectively; particles outside of these are not shown.

parastichy. If the applied torsion is removed immediately after this reaction, the dislocations will remain in this orientation and move apart to a state with maximum azimuthal separation. By reversing the direction of torsion (state 3), we then cause dislocations to glide toward a configuration in which they can react along a $\pm\mathbf{a}_2$ parastichy (state 4) and change their orientation once again, this time to the third possible direction $\pm\mathbf{a}_3$ (state 5). Finally, upon removal of the applied torsion, the dislocations glide to maximize their azimuthal separation and reach a metastable state (state 6, Supplemental Material video 4 [49]).

IV. CONCLUSION

To elucidate the complex interplay between topological defects, lattice chirality, and surface geometry in freestanding tubular crystals, we have employed MD simulations to investigate the behavior of patchy particles, organized into tubular structures with pre-existing defects. In agreement with predictions made using elastic network simulations [19], our study finds the emergence of stable dislocation patterns, a behavior specific to tubular crystals, causing significant deformations

in the macroscopic shape of the crystal. Beyond the scope of the previous elastic network approach, our MD simulations here also reveal novel sequences of dislocation reaction events that are distinctive to tubular crystals. Even when the existing defects are positioned several lattice spacings apart, they exhibit reactions "at a distance," through nucleation and glide-separation of reaction-mediating dislocation pairs, that lead to changes in their orientations. Consequently, this alteration in the orientation of dislocations induces transformations in the helicity of the lattice. In addition, the vacancy formation and particle extrusion events observed in our molecular-dynamics simulations represent a class of irreversible rearrangements, not accessible to the elastic network model or to continuum elasticity calculations, and they could provide target sites for hierarchical assembly bonds or nucleation sites for secondary crystalline layers.

In contrast to continuum elastic models for tubular structures, including those with anisotropic elasticity and localized stresses associated with the presence of defects, our coarse-grained model inherently incorporates the discreteness of lattice orientation distinctive to tubular crystals. Unbinding and motion of dislocations in a crystalline lattice usually take place along the primitive lattice directions, which in a tubular crystal depend on the lattice helicity. The resulting paths of dislocation motion do not always follow the direction of largest stress. Our model predicts that in armchair tubes under torsion, dislocations unbind and glide along the tube axis, even when this direction is farther from the direction of maximum stress compared to other primitive lattice directions. While continuum elasticity calculations provide useful insights into dislocation glide motion (as in Fig. 5), our MD simulations indicate that tubular crystals can exhibit a wealth of higher-order defect transformations that require discrete-particle models to simulate.

Our investigation establishes externally applied torsion as a promising means to effectively regulate the dislocation motion. We show that time-varying manipulation of the direction and magnitude of these forces can be used to initiate a sequence of elementary reactions that result in a desired dislocation reorientation, defect pattern, and change in crystal helicity. This controllable design of dislocation dynamics holds the potential to engineer colloidal crystal assemblies with *in situ*–tunable mechanical and electro-optic properties. Despite the strong assumptions underlying the analytical theory of Ref. [54], we found that it generated useful predictions for dislocation glide both before and after a dislocation reaction. Our findings indicate a need for an extension to this theory that can systematically predict which geometrically possible dislocation reactions will be energetically favorable.

Our results suggest that it would be fruitful in future work to examine dislocation reaction sequences on 2D crystals of other periodic topologies, such as spherical [58], toroidal [59], or conical [60], and on tubular crystals with helicities other than the (near-)armchair configurations that we have studied here. How these dislocation reaction sequences may influence the kinetics of tubular crystal self-assembly remains an open question. Slight variations to our patchy particle construction could offer future simulations a minimal model of tubular crystals with spontaneous curvature, preferred helicity, and/or

crystal symmetries other than hexagonal, e.g., modeling the rhombic lattices of tubulin that make up microtubules [61] or potential colloidal analogs [62,63].

Altogether, our findings not only offer insights into the rich interplay between topological defects, lattice helicity, and surface geometry at play in freestanding tubular crystals, but they also advance our understanding of dislocation behavior in flexible 2D crystals and the variety of ways in which they can interact.

[1] M. A. Lohr, A. M. Alsayed, B. G. Chen, Z. Zhang, R. D. Kamien, and A. G. Yodh, Helical packings and phase transformations of soft spheres in cylinders, Phys. Rev. E **81**, 040401(R) (2010).

[2] A. Mughal, H. K. Chan, D. Weaire, and S. Hutzler, Dense packings of spheres in cylinders: Simulations, Phys. Rev. E **85**, 051305 (2012).

[3] D. Wood, C. Santangelo, and A. Dinsmore, Self-assembly on a cylinder: a model system for understanding the constraint of commensurability, Soft Matter **9**, 10016 (2013).

[4] N. Tanjeem, W. H. Wilkin, D. A. Beller, C. H. Rycroft, and V. N. Manoharan, Geometrical frustration and defect formation in growth of colloidal nanoparticle crystals on a cylinder: Implications for assembly of chiral nanomaterials, ACS Appl. Nano Mater. **4**, 10682 (2021).

[5] H. Liu, Y. Zong, M. Zu, T. G. Mason, F. Ye, and K. Zhao, Curvature-assisted self-assembly of Brownian squares on cylindrical surfaces, J. Colloid Interface Sci. **605**, 863 (2022).

[6] B. I. Yakobson and P. Avouris, Mechanical properties of carbon nanotubes, in *Carbon Nanotubes: Synthesis, Structure, Properties, and Applications*, Topics in Applied Physics Vol. 80 (Springer, Heidelberg, 2001), pp. 287–327.

[7] D. A. Beller and D. R. Nelson, Plastic deformation of tubular crystals by dislocation glide, Phys. Rev. E **94**, 033004 (2016).

[8] P. M. Ajayan and O. Z. Zhou, Applications of carbon nanotubes, in *Carbon Nanotubes: Synthesis, Structure, Properties, and Applications*, Topics in Applied Physics Vol. 80 (Springer, Heidelberg, 2001), pp. 391–425.

[9] R. H. Baughman, A. A. Zakhidov, and W. A. De Heer, Carbon nanotubes–the route toward applications, Science **297**, 787 (2002).

[10] A. Klug, The tobacco mosaic virus particle: structure and assembly, Philos. Trans. R. Soc. London B **354**, 531 (1999).

[11] E. Nogales, Structural insights into microtubule function, Annu. Rev. Biochem. **69**, 277 (2000).

[12] D. Hayakawa, T. E. Videbaek, D. M. Hall, H. Fang, C. Sigl, E. Feigl, H. Dietz, S. Fraden, M. F. Hagan, G. M. Grason *et al.*, Geometrically programmed self-limited assembly of tubules using DNA origami colloids, Proc. Natl. Acad. Sci. USA **119**, e2207902119 (2022).

[13] Y. Wu, X. Zhao, Y. Shang, S. Chang, L. Dai, and A. Cao, Application-driven carbon nanotube functional materials, ACS Nano **15**, 7946 (2021).

[14] F. Wang, S. Zhao, Q. Jiang, R. Li, Y. Zhao, Y. Huang, X. Wu, B. Wang, and R. Zhang, Advanced functional carbon nanotube fibers from preparation to application, Cell Rep. Phys. Sci. **3**, 100989 (2022).

[15] H. Gu, E. Hanedan, Q. Boehler, T.-Y. Huang, A. J. Mathijssen, and B. J. Nelson, Artificial microtubules for rapid and collective transport of magnetic microcargoes, Nat. Mach. Intell. **4**, 678 (2022).

[16] H. Ijaz, A. Mahmood, M. M. Abdel-Daim, R. M. Sarfraz, M. Zaman, N. Zafar, S. Alshehery, M. M. Salem-Bekhit, M. A. Ali, L. B. Eltayeb *et al.*, Review on carbon nanotubes (CNTs) and their chemical and physical characteristics, with particular emphasis on potential applications in biomedicine, Inorg. Chem. Commun. **155**, 111020 (2023).

[17] T. Dumitrica, M. Hua, and B. I. Yakobson, Symmetry-, time-, and temperature-dependent strength of carbon nanotubes, Proc. Natl. Acad. Sci. USA **103**, 6105 (2006).

[18] L. Zhu, J. Wang, and F. Ding, The great reduction of a carbon nanotube's mechanical performance by a few topological defects, ACS Nano **10**, 6410 (2016).

[19] A. Zakharov and D. A. Beller, Shape multistability in flexible tubular crystals through interactions of mobile dislocations, Proc. Natl. Acad. Sci. USA **119**, e2115423119 (2022).

[20] V. I. Artyukhov, E. S. Penev, and B. I. Yakobson, Why nanotubes grow chiral, Nat. Commun. **5**, 4892 (2014).

[21] G. D. Förster, V. Pimonov, H.-N. Tran, S. Tahir, V. Jourdain, and C. Bichara, Swinging crystal edge of growing carbon nanotubes, ACS Nano **17**, 7135 (2023).

[22] N. Vogel, M. Retsch, C.-A. Fustin, A. Del Campo, and U. Jonas, Advances in colloidal assembly: the design of structure and hierarchy in two and three dimensions, Chem. Rev. **115**, 6265 (2015).

[23] Y.-J. Kim, J.-B. Moon, H. Hwang, Y. S. Kim, and G.-R. Yi, Advances in colloidal building blocks: toward patchy colloidal clusters, Adv. Mater. **35**, 2203045 (2023).

[24] Z. Gong, T. Hueckel, G.-R. Yi, and S. Sacanna, Patchy particles made by colloidal fusion, Nature (London) **550**, 234 (2017).

[25] Y. Wang, Y. Wang, D. R. Breed, V. N. Manoharan, L. Feng, A. D. Hollingsworth, M. Weck, and D. J. Pine, Colloids with valence and specific directional bonding, Nature (London) **491**, 51 (2012).

[26] T. Zhang, D. Lyu, W. Xu, Y. Mu, and Y. Wang, Programming self-assembled materials with DNA-coated colloids, Front. Phys. **9**, 672375 (2021).

[27] Z. Zhang and S. C. Glotzer, Self-assembly of patchy particles, Nano Lett. **4**, 1407 (2004).

[28] K. Van Workum and J. F. Douglas, Symmetry, equivalence, and molecular self-assembly, Phys. Rev. E **73**, 031502 (2006).

[29] É. Duguet, C. Hubert, C. Chomette, A. Perro, and S. Ravaine, Patchy colloidal particles for programmed self-assembly, C. R. Chim. **19**, 173 (2016).

[30] S. Ravaine and E. Duguet, Synthesis and assembly of patchy particles: Recent progress and future prospects, Curr. Opin. Colloid Interface Sci. **30**, 45 (2017).

[31] J. D. Weeks, D. Chandler, and H. C. Andersen, Role of repulsive forces in determining the equilibrium structure of simple liquids, J. Chem. Phys. **54**, 5237 (1971).

[32] J. E. Lennard-Jones, Cohesion, Proc. Phys. Soc. **43**, 461 (1931).

[33] X. Wang, S. Ramírez-Hinestrosa, J. Dobnikar, and D. Frenkel, The Lennard-Jones potential: when (not) to use it, Phys. Chem. Chem. Phys. **22**, 10624 (2020).

[34] É. Ducrot, M. He, G.-R. Yi, and D. J. Pine, Colloidal alloys with preassembled clusters and spheres, Nat. Mater. **16**, 652 (2017).

[35] R. A. M. Kalapurakal, B. C. Rocha, and H. Vashisth, Self-assembly in an experimentally realistic model of lobed patchy colloids, ACS Appl. Bio Mater. **7**, 535 (2024).

[36] S. Plimpton, Fast parallel algorithms for short-range molecular dynamics, J. Comput. Phys. **117**, 1 (1995).

[37] M. Dresselhaus, G. Dresselhaus, and R. Saito, Physics of carbon nanotubes, Carbon **33**, 883 (1995).

[38] T. Nishihara, A. Takakura, K. Matsui, K. Itami, and Y. Miyauchi, Statistical verification of anomaly in chiral angle distribution of air-suspended carbon nanotubes, Nano Lett. **22**, 5818 (2022).

[39] B. I. Yakobson, C. J. Brabec, and J. Bernholc, Nanomechanics of carbon tubes: instabilities beyond linear response, Phys. Rev. Lett. **76**, 2511 (1996).

[40] Q. Wang, Effective in-plane stiffness and bending rigidity of armchair and zigzag carbon nanotubes, Int. J. Solids Struct. **41**, 5451 (2004).

[41] Q. Lu, M. Arroyo, and R. Huang, Elastic bending modulus of monolayer graphene, J. Phys. D **42**, 102002 (2009).

[42] C. D. Zeinalipour-Yazdi and E. Z. Loizidou, Study of the cap structure of (3, 3), (4, 4) and (5, 5)-SWCNTs: Application of the sphere-in-contact model, Carbon **115**, 819 (2017).

[43] J. Lidmar, L. Mirny, and D. R. Nelson, Virus shapes and buckling transitions in spherical shells, Phys. Rev. E **68**, 051910 (2003).

[44] R. Zandi, D. Reguera, R. F. Bruinsma, W. M. Gelbart, and J. Rudnick, Origin of icosahedral symmetry in viruses, Proc. Natl. Acad. Sci. USA **101**, 15556 (2004).

[45] G. Vernizzi and M. Olvera de la Cruz, Faceting ionic shells into icosahedra via electrostatics, Proc. Natl. Acad. Sci. USA **104**, 18382 (2007).

[46] I. García-Aguilar, P. Fonda, E. Sloutskin, and L. Giomi, Faceting and flattening of emulsion droplets: A mechanical model, Phys. Rev. Lett. **126**, 038001 (2021).

[47] A. Chuvilin, U. Kaiser, E. Bichoutskaia, N. A. Besley, and A. N. Khlobystov, Direct transformation of graphene to fullerene, Nat. Chem. **2**, 450 (2010).

[48] V. B. Shenoy, C. D. Reddy, and Y.-W. Zhang, Spontaneous curling of graphene sheets with reconstructed edges, ACS Nano **4**, 4840 (2010).

[49] See Supplemental Material at http://link.aps.org/supplemental/10.1103/PhysRevMaterials.8.055601 for descriptions of Supplemental Material Videos.

[50] S. J. Gerbode, S. H. Lee, C. M. Liddell, and I. Cohen, Restricted dislocation motion in crystals of colloidal dimer particles, Phys. Rev. Lett. **101**, 058302 (2008).

[51] L. Kubin, *Dislocations, Mesoscale Simulations and Plastic Flow* (Oxford University Press, USA, 2013), Vol. 5.

[52] W. T. Irvine, A. D. Hollingsworth, D. G. Grier, and P. M. Chaikin, Dislocation reactions, grain boundaries, and irreversibility in two-dimensional lattices using topological tweezers, Proc. Natl. Acad. Sci. USA **110**, 15544 (2013).

[53] J. P. Hirth and J. Lothe, *Theory of Dislocations*, 3rd ed. (Wiley, New York, 1982).

[54] A. Amir, J. Paulose, and D. R. Nelson, Theory of interacting dislocations on cylinders, Phys. Rev. E **87**, 042314 (2013).

[55] S. K. Tiwari, S. K. Pandey, R. Pandey, N. Wang, M. Bystrzejewski, Y. K. Mishra, and Y. Zhu, Stone–Wales defect in graphene, Small **19**, 2303340 (2023).

[56] L. Yang, M. P. Anantram, J. Han, and J. P. Lu, Band-gap change of carbon nanotubes: Effect of small uniaxial and torsional strain, Phys. Rev. B **60**, 13874 (1999).

[57] J. Charoenpakdee, O. Suntijitrungruang, and S. Boonchui, Chirality effects on an electron transport in single-walled carbon nanotube, Sci. Rep. **10**, 18949 (2020).

[58] C. Negri, A. L. Sellerio, S. Zapperi, and M. C. Miguel, Deformation and failure of curved colloidal crystal shells, Proc. Natl. Acad. Sci. USA **112**, 14545 (2015).

[59] M. J. Bowick and L. Giomi, Two-dimensional matter: order, curvature and defects, Adv. Phys. **58**, 449 (2009).

[60] H. Ansell, A. Tomlinson, and N. Wilkin, Transitions between phyllotactic lattice states in curved geometries, Sci. Rep. **10**, 17411 (2020).

[61] S. Cheng and M. J. Stevens, Self-assembly of chiral tubules, Soft Matter **10**, 510 (2014).

[62] F. Li, X. Badel, J. Linnros, and J. B. Wiley, Fabrication of colloidal crystals with tubular-like packings, J. Am. Chem. Soc. **127**, 3268 (2005).

[63] V. N. Manoharan, Colloidal matter: Packing, geometry, and entropy, Science **349**, 1253751 (2015).